ADVANCED ENGINEERING MATERIALS

DOI: 10.1002/adem.201600721

Simulation of Short Fatigue Crack Propagation in a 3D Experimental Microstructure**

By *Henry Proudhon,* J. Li, Wolfgang Ludwig, Arjen Roos#* and *Samuel Forest*

A three dimensional simulation of short fatigue crack propagation in a polycrystalline microstructure using a crystal plasticity finite element model is carried out. The experimental microstructure which contains several hundreds grains, was obtained via diffraction contrast tomography. A step-by-step short fatigue crack growth model based on capturing the plastic activity at the crack tip is used. Technical details are given and discussed in light of the compromise needed to perform such demanding calculations. The crack propagates through several grains and depicts some of the characteristic short crack features observed experimentally in the literature.

1. Introduction

Short fatigue crack propagation in the first few grains of a polycrystalline microstructure remains extremely challenging to model and predict although in many cases, it may represent a very significant portion of a component's life.[1] The microstructural variability in the initiation part has received a lot of attention, and recently has seen a regain of interest with the new availability of three dimensional (3D) microstructure characterization tools together with the possibility to carry out large scale crystal plasticity simulations. This lead to some real advances in our understanding of fatigue crack initiation, as well as in our ability to predict it.[2–4]

On the other hand, regarding the subsequent stage I propagation which is a 3D process by nature, there is still a lack of experimental data and most of the short crack growth models are phenomenological and cannot assess the experimental scatter observed.[5–7] Experimentally, the increasing use of 3D non-destructive techniques, such as X-ray tomography is an important step forward to study in situ, the propagation of fatigue cracks in three dimensions.[8–10] Coupled to a detailed knowledge of the microstructure, this might just be the experimental combination needed to pin point the underlying physical mechanisms of the crack growth process.[11,12] One of the issues with this technique is that the spatial resolution routinely available and compatible with millimetric sized specimens lies between 0.1 and 1.0 micron, which is usually not enough to resolve the very fine step of the crack switching from one crystallographic plane to another. One way forward is to add a subsequent characterization step at the end of the in situ experiment, which is usually destructive, but with a much higher resolution to assess the details of the crack at a finer scale.[13,14] Interesting alternatives, such as SEM-based fractography combined with X-ray diffraction microscopy were recently investigated.[15] Femtosecond laser ablation coupled to EBSD Tribeam experiments also appear as an interesting route to complement in situ X-ray tomography experiments.[16,17]

Even with such detailed experiments, the growth behavior remain difficult to analyze, since the stress state or the plastic activity at the crack tip for a given number of cycles remain unknown. One promising route seems, thus, to couple detailed 3D experiments with microstructure sensitive CPFE computations – including the crack geometry – to account for the stress and plastic strain redistribution. Indeed, the general way to look at this problem is to compute some fatigue indicator parameters (FIP), which are to be regarded as crack formation driving forces. They have been used extensively for predicting the initiation phase[18–22] and are gaining traction for the stage I propagation phase analysis. Using extensive sets of calculations with single crystals containing cracks, Castelluccio and McDowell showed that computed FIPs are directly proportional to the crack sliding displacement, which is one of the principal driving forces for stage I crack growth.[23]

[*] *Dr. H. Proudhon, Dr. J. Li, Dr. S. Forest*
MINES ParisTech, PSL Research University, MAT - Centre des matériaux, CNRS, UMR 7633, BP 87 91003 Evry, France
E-mail: henry.proudhon@mines-paristech.fr
Dr. W. Ludwig
MATEIS, INSA de Lyon, Université de Lyon, Villeurbanne 69621, France
European Synchrotron Radiation Facility, Grenoble 38043, France
Dr. A. Roos
Onera, the French Aerospace Lab, France
A. Roos present address is Safran Tech – Paris Saclay, France

[**] *This work was carried out under the French ANR Project CRYSTAL 2010-BLAN-91801.*

In spite of this, due to a lack of experimental comparisons, it is presently not clear if those predictions based on the FIP distributions are really accurate. One of the reasons is the technical limitations to describe at the same time the geometry of the crack, the microstructural features, a large enough volume of material to avoid side effects, and the simulation of many fatigue cycles. However, recent advances in all of those aspects allow to move forward. The 3D characterization of millimetric polycrystalline microstructure is now available using serial sectioning techniques (destructive) or near-field synchrotron X-ray diffraction imaging (non-destructive and in a close future using laboratory sources[24]). Meshing complex microstructural 3D images is also considerably easier, thanks to the development of new tools, see Proudhon et al. and Spear et al.,[25,26] for examples. Using adequate remeshing routines, it is possible to study the propagation of short cracks based on some FIP indicator.[27] Although there have been some attempts in 2D[28] and more recently in 3D,[29,30] the simulation of the propagation has never been done using an experimental 3D polycrystalline microstructure.

The model described in Proudhon et al.[27] was previously used only with single crystal configurations using a different combinations of slip systems in the mechanical behavior, which showed the capability to predict both crystallographic and tortuous crack paths. The purpose of this paper is to apply the same methodology with an experimentally measured 3D microstructure and propagate a crack through several grains.

The paper is divided into two main parts, the first one describes the 3D material characterization and the numerical methods used to simulate the crack propagation. The second part presents the results of the short crack propagation simulation in the experimental microstructure.

2. Materials and Methods

2.1. Three Dimensional Experimental Microstructure

A VST55531 material coupon was used for the tomographic acquisition. It is a near-β (body centered cubic crystal structure) titanium alloy with additions of 5% Al, V, and Mo, 3% Cr, and 1% Zr (weight%). The sample studied in this work was annealed at 843 °C for 2 h under vacuum and then air cooled (the β transus temperature is slightly above 800 °C). After the heat treatment, a fully static recrystallisation of the β phase was obtained with a mean grain diameter of 65 μm and an orientation spread per grain around 0.2°.

The 3D grain structure was captured by Diffraction Contrast Tomography (DCT) carried out at the id19 beamline at the European Synchrotron. A box monochromatic X-ray beam with an energy of 35.3 keV slitted down to $600 \times 600\ \mu m^2$ was used to illuminate the central region of the specimen (see Figure 1 left). A high resolution 2048×2048 pixels Frelon detector placed 4 mm downstream the specimen was used to record both the transmitted beam and the diffracted beams. The effective pixel size was 1.4 μm giving a field of view of $2.8 \times 2.8\ mm^2$, allowing to capture simultaneously the direct beam and several {hkl} families of diffraction spots. Seven thousand two-hundred projections were continuously recorded over the 360° rotation and subsequently processed by the DCT code to segment the spots, do the pair matching, index, and reconstruct each grain.[31,32] Finally, a 3D isotropic dilation is conducted to fill in the residual voids that may exist between reconstructed grains. The precision of the grain boundary with the present setup has been previously estimated to 2 μm.[32] The reconstructed data set is a 3D volume of the grain labels, in the (XYZ) laboratory coordinate system (see Figure 1 left). Each label is complemented by the mean grain orientation from the diffraction indexing, in the form of a Rodrigues vector expressed in (XYZ), which can be transformed into Euler angles. The same coordinate system will be used for the simulation. The specimen was later subjected to fatigue testing, which could be used in the future to confront the present simulations. Here, we are interested only in the experimental initial microstructure to serve as input for the finite element calculation.

2.2. Material Mechanical Behavior

To identify the constitutive behavior of the material, tension-compression tests were carried out using axisymmetric specimens fitted with a 120 Ω resistance strain gauge mounted on the surface to measure accurately the axial strain within the range of ±2%. The experimental test database was made of strain-controlled monotonic tensile tests with different strain rates, as well as cyclic tension-compression tests performed either in stress control or in strain control, with a strain rate of $\dot{\varepsilon} = 10^{-4}\ s^{-1}$.

Stress-controlled tests were carried out using the same strain rate, while monitoring the maximum and minimum stresses with $\sigma_{max} = 1150$ MPa and $\sigma_{min} = -1100$ MPa. Ratchetting progressively takes place in the first five cycles and stabilizes with plastic strain accumulation per cycle of $\delta\varepsilon_p = 0.02\%$ until the strain gage fails at 2% strain. Cyclic strain-controlled tensile-compression tests were conducted with an imposed strain range of $\varepsilon = \pm 1.3\%$ and cyclic softening is observed in that case.

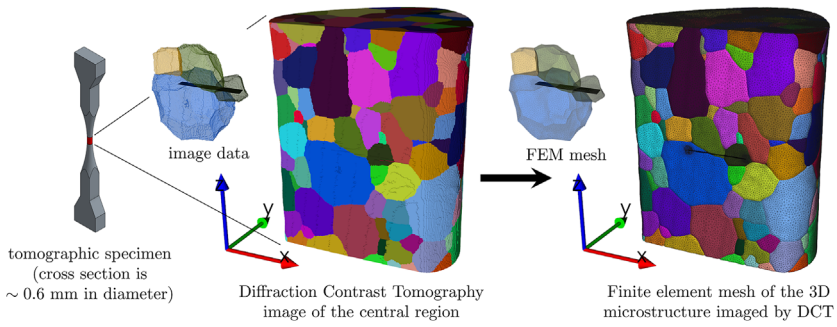

Fig. 1. Tetrahedron-based meshing of the 55531 β-Ti microstructure imaged by DCT, a pre-crack in inserted into the mesh, which is refined around the crack tip, as detailed in section 2.5; a close-up view of some of the grains of interest is shown both for image data and the corresponding FEM mesh.

ADVANCED ENGINEERING MATERIALS 2017,
DOI: 10.1002/adem.201600721

The material parameters are identified by comparing the experimental results to FE simulations using a 3D Voronoï aggregate of 100 randomly oriented grains with periodic boundary conditions, which was considered as a Representative Volume Element (RVE) of the material.

The constitutive behavior adopted, here, is a classical phenomenological crystal plasticity Meric-Cailletaud model.[33,34] The model was detailed previously,[27] only the parts relevant to this study (anisotropic elasticity and work hardening rules) are explained in detail here. The total strain tensor $\varepsilon_{\sim}$ is partitioned into an elastic part $\varepsilon^{e}_{\sim}$ and a plastic part $\varepsilon^{p}_{\sim}$. Regarding elasticity, the material VST55531 having a cubic crystal structure, cubic elasticity is used with $C_{11} = 167\,000$ MPa, $C_{12} = 115\,000$ MPa and $C_{44} = 44\,000$ MPa in Voigt's notation.[35] The homogenised Young's modulus for the RVE is 98 500 MPa.

The plastic strain is the result of the possible activation of N slip systems. To limit the number of degrees of freedom of the simulation, only the 12 {110}⟨111⟩ (2 ⟨111⟩ directions for each of the 6 {110} planes) slip systems are considered here. Each system s can produce some slip γ^s, when the resolved shear stress τ^s, corrected from isotropic and kinematic work hardening, exceeds a critical value τ_0. The corresponding slip rate is obtained through the following equation:

$$\dot{\gamma}^s = \mathrm{sign}(\tau^s - x^s)\left\langle \frac{|\tau^s - x^s| - r^s - \tau_0}{K} \right\rangle^n, \quad (1)$$

where $\langle x \rangle = \max(x,0)$. Both work hardening sets of variables r^s and x^s (initially zero) are computed from the state laws:

$$r^s = Q\sum_{r=1}^{N} H^{rs}\rho^s, \quad \text{and} \quad x^s = C\alpha^s \quad (2)$$

The state variables ρ^s and α^s are associated with the dislocation densities responsible for the work hardening (isotropic and kinematic respectively) and evolve as the plastic slip occurs in the material, thanks to the following non linear laws:

$$\dot{\rho}^s = (1 - b\rho^s)|\dot{\gamma}^s|, \quad \text{and} \quad \dot{\alpha}^s = \left(\mathrm{sign}(\tau^s - x^s) - D\alpha^s\right)|\dot{\gamma}^s| \quad (3)$$

The retained parameters are listed in Table 1, and the comparison of the obtained constitutive behavior for the 100 grains RVE with the cyclic tension-compression tests is depicted in Figure 2. The negative value of Q reproduces correctly the stress softening observed experimentally and the non-linear kinematic hardening leads to ratcheting, when the stress-controlled tension-compression cycles are not centered. The corresponding value, when $\sigma_{max} = 1150$ MPa and $\sigma_{min} = -1100$ MPa is $\delta\varepsilon^r_p = 0.023\%$ per cycle. On a side note, the transition from elasticity to plasticity in the tensile curve is not perfectly identified (not shown here), which is a rather typical fact when fitting both monotonic and cyclic tests. This could be improved, typically by increasing the number of kinematic hardening components. However, this is not critical to our analysis and to keep down the complexity of the material model, only one kinematic hardening component is considered. The value of τ_0 has also been kept down, in order to account for the micro-plasticity in the grains. Indeed, the plastic activity, at the crack, tip is an essential component for fatigue crack propagation and will be the driving force in our damage indicator. Overall, the identified parameters allow a good description of the macroscopic behavior including the observed stress softening and plastic strain ratcheting.

Table 1. Identified crystal plasticity constitutive material parameters for Ti55531.

Viscosity		Isotropic hardening				Kinematic hardening	
K [MPa s^{-9}]	n	τ_0 [MPa]	Q [MPa]	b	H^{rs}	C [MPa]	D
100	5	150	–30	30	1	450 000	1 400

2.3. Overview of the Model

To achieve the propagation of short cracks informed by microstructural features, a series (hereafter called steps) of large scale finite element crystal plasticity computations are carried out using the following four ingredients:

1) an accurate description of a 3D experimental microstructure (see sections 2.1 and 2.4);
2) a finely calibrated crystal plasticity model (see section 2.2);
3) robust state of the art meshing tools to describe and update the crack geometry and refine the mesh, where it is needed to capture the plastic activity at the crack tip (see section 2.5);
4) a damage indicator defined by post-processing the state variables to predict the local crack propagation direction and growth rate.

Combining these ingredients and computing a limited number of fatigue cycles for a given step, the plastic strain fields in the vicinity of the crack tip can be predicted

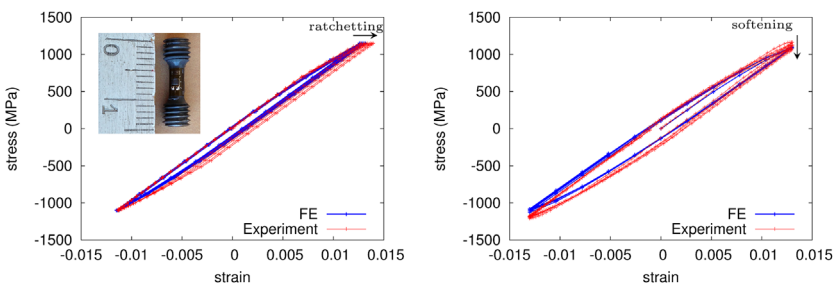

Fig. 2. Simulation results of a cyclic stress controlled test (left) and a strain controlled test (right), the inset shows the specimen type used for the tests.

accurately. Here, the damage indicator D is closely related to the FIPs previously defined in the literature. It is similar to the D_5 metrics used by Hochhalter,[20] but is expressed in stress units and includes explicitly a contribution of the resolved shear stress. Most of the FIP based on plastic slip gives a similar field and would lead to the same results. In the absence of direct 3D comparison with experimental results, a comparative study was not appropriate and a single damage indicator was used throughout this work. At each integration point and at each time increment, the damage indicator D is obtained by the maximum value among the slip systems of the following combination of γ^s, τ^s, and σ_n^s:

$$D(t) = \max_{s\in[[1,N]]} \int_0^t |\dot{\gamma}^s| \left(|\tau^s| + k\langle \sigma_n^s \rangle \right) dt, \tag{4}$$

where k is a dimensionless parameter set to 0.4, which controls the damage sensitivity to the stress normal to the slip plane. At the end of each step, the damage indicator field is, then, computed by post-processing these values to predict the direction and the local crack growth rate at each point of the crack front.

The methodology can be summarised as follows: From CPFE computations of a cracked body, the damage indicator D (cf. Eq. 4), based on the accumulated slip, the resolved shear stress and the normal stress on each slip system are calculated at each integration point and for every time increment. The crack growth direction is, then, determined by analyzing this damage indicator in the region around the crack front. The crack is extended via remeshing at each propagation event. At this point, the state variables can be transferred to the new mesh corresponding to the new crack configuration (see Branco et al.[36] for a recent review on the use of adaptive remeshing techniques to simulate crack growth). The CPFE computation is then continued at the next step. More details concerning this methodology can be found in previous papers.[27,37]

The main difference with the previous application of the model deals with the size of the computations, related to the use of a 3D experimental microstructure. Combining a significant volume of the material, so that the crack is located far enough from the boundary conditions and a mesh size at the crack tip sufficiently small to accurately capture the plastic activity remains challenging. An efficient numerical method through Multiple Point Constraints (MPC, not detailed here for brevity) has been employed to use only quadratic elements in the vicinity of the crack and linear elements everywhere else. In spite of this, the calculations feature about 20 millions degrees of freedom, which requires the use of parallel computing. In addition, in this work, due to the size of the computation, each propagation step correspond to one fatigue cycle, and the critical value D_c of the damage indicator was arbitrarily set to 0.1 MPa allowing to evaluate the D field and to propagate the crack to the next step. Furthermore, due to present technical limitations with the parallel computing in our finite element code, the plastic strain field was not transferred from one step to the next (see Proudhon et al.[27] for more details).

Regarding the number of cycles to simulate per step, it is useful to note that for a given crack geometry, when the situation is stabilized, the values of D will just increase linearly cycle after cycle. In that sense D_c is related to a critical damage per cycle to propagate the crack through a given distance. In the general case, because the material behavior evolves with work hardening, a few cycles have to be simulated to obtain a good estimation of this stabilized state (for instance Musinski et al. simulate 3 fatigue cycles in their work[21]). Due to the size of the computation, only one cycle is simulated at each step, which may limit the accuracy of the present simulation. Despite all of these limitations, this works represents a significant step toward the modeling and simulation of the propagation of short cracks.

2.4. Meshing the Experimental Microstructure

The reconstructed data set is composed of 387 grains with a grain size of approximately 65 μm. First, the full image data is meshed as described in Proudhon et al.[25] to obtain a tetrahedron-based representation of the gage length of the specimen. At this stage, all the grains have been meshed, the grain size and grain boundary precision can be checked quantitatively with respect to initial image data and are in excellent agreement: the grain size matches within 1% and the grain boundary precision matches mostly within 1 pixel = 1.4 μm. Tetrahedrons are grouped into element sets named by the experimental grain label, so that the grain orientations can be specified accordingly.

2.5. Crack Insertion into the Mesh

The fatigue crack propagation model needs an initial crack as a starting point. In this work, a rectangular pre-crack is inserted within the mesh. This crack corresponds to a small FIB notch located in the sample to control the crack initiation in the experiment. The precise geometry is available from the tomographic image (141 μm along X and 26 μm along Y) and has been used to define the initial defect. A surface mesh of the pre-crack is created and, then, inserted automatically into the 3D polycrystalline mesh using Z-cracks,[38,39] a module of the Z-set software suite (internally this process uses a combination of Yams, Meshadapt and Ghs3d distributed by Distène). The main steps of crack insertion (see Figure 3) are detailed in the next paragraph:

1) First, the surface crack geometry is meshed independently, but in the same coordinate system as the volume mesh in which the crack is inserted.
2) Second, the volume mesh of the polycrystal is refined in the region, where the crack will be inserted. The element size of the refined mesh is determined from the distance to the nearest node in the crack surface mesh. This process eases the next step, which involves boolean operations and needs a minimal mesh density.

DOI: 10.1002/adem.201600721

3) Next, the adapted volume mesh is cut by the surface mesh of the crack using boolean operations. Then, it is remeshed several times (note that the grain boundary geometry is preserved during this process) to achieve the desired mesh refinement around the crack tip. The remeshing process is carried out by defining the minimum edge length l near the crack front and a coarsening factor h that specifies the maximum edge length variation between adjacent elements. A mesh sensitivity analysis was carried out previously with single crystals calculations[27] and showed that results converged with sub-micron element size. In the present work, the cracks were meshed using $l = 0.1$ μm and $h = 1.1$. This lead to elements smaller than 1 μm in a 10 micron tore radius from the crack tip.
4) Finally, after the last remeshing operation, the grain numbers are reassigned to the cracked mesh based on their position with respect to the reconstructed image data set.

3. Simulation of Short Fatigue Crack Propagation in the Experimental Microstructure

The complete mesh is partitioned into 32 sub-domains handled during the computation by a FETI parallel computing algorithm.[40] At each iteration, the local sub-problems are solved independently and simultaneously. At the boundary nodes, Lagrange multipliers are introduced to enforce continuity of the displacements. Next, a parallel conjugate projected gradient algorithm is applied to determine the Lagrange multipliers that represent the interaction forces at the boundary. The load was imposed thanks to a cyclic vertical displacement of the top surface while maintaining no vertical displacement at the bottom. The maximum displacement was 1.65 mm, which corresponds to a tensile load of 45 N (average stress of 300 MPa) and a stress ratio of 0.1 was used. Some degrees of freedom were also suitably blocked in order to prevent rigid body motions.

Each step took between 3 (initial step) to 5 (final step) days (wall-clock time) to compute. The post-processing time to output and process the distributions of D at the crack front was only a few minutes and can be considered negligible. Execution time of the various meshing and remeshing operations remained below one hour for each step.

3.1. Propagation from the Initial Pre-Crack

The initial pre-crack is located into three grains: grain 6, grain 52, and grain 221 (see Table 2 for their respective orientation and also close-up view in Figure 1 for their location). Note, that the crack front in grain 221 is close to the grain boundary both at the sample surface and in the bulk.

The first propagation step is carried out as detailed in section 2. The accumulated plastic strain at the surface of the sample after the first step (i.e., after one fatigue cycle simulated at 300 MPa with the pre-crack geometry and before propagating the crack), is shown in Figure 4. In this figure, the traces of some active slip planes on both sides of the pre-crack are drawn in a close-up view of the crack tips. The corresponding values of the activated slip systems for the two grains, as well as the computed values of the damage indicator are also shown. It can be observed that in grain 6, one slip band localises along the (101) plane, another slip band localises along a combination of $(\bar{1}01)$ and (110) slip planes, of which the $(\bar{1}01)$ slip plane has the maximum Schmid factor with respect to the macroscopic load. In grain 221, the slip localizes mainly along a combination of (101) and (011) slip planes. In contrast, the $(\bar{1}01)$ slip plane that has the maximum Schmid factor shows almost no plastic activity.

The above analysis confirms that the slip activity and the mixed loading mode at the crack tip in such a polycrystal is very complex. In particular, the macroscopic Schmid factor (which assumes uniaxial loading) cannot give a good estimation of the slip activation at the crack tip. This is in agreement with previous experimental observations suggesting that contrary to crack initiation, the macroscopic Schmid factor is not a primary factor for short crack

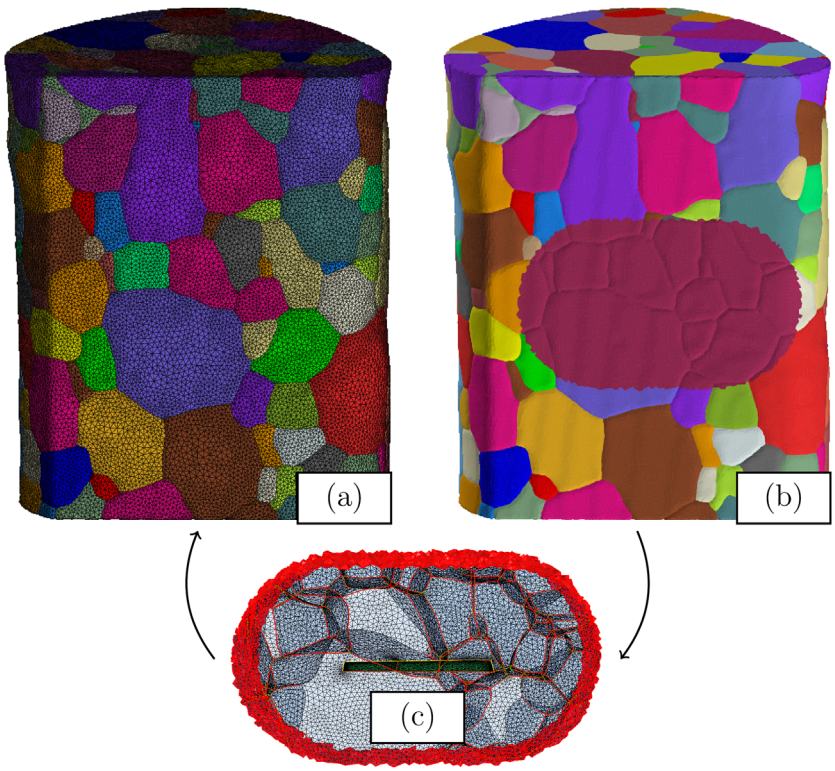

Fig. 3. Details of the crack insertion preserving the grain boundary information: (a) the polycrystalline mesh reconstructed from the tomographic images (b) a region of 100 μm around the notch is extracted, based on the crack geometry (c) a 3D view of the remeshed region with the notch inserted.

Table 2. Orientation of the grains where the pre-crack is located, the sample reference frame (X, Y, Z) in which the Euler angles are expressed is shown in Figure 1; the highest Schmid Factor (SF) with respect to the macroscopic load with the corresponding slip system is also indicated.

Grain	ϕ_1 [°]	Φ [°]	ϕ_2 [°]	Highest SF	System
6	142.8	32.0	214.4	0.461	$(\bar{1}01)[1\bar{1}1]$
52	196.4	3.7	202.4	0.431	$(\bar{1}01)[1\bar{1}1]$
221	81.1	25.4	291.1	0.496	$(011)[11\bar{1}]$

propagation.[11,12] Although, due to its attractive simplicity and the fact, that it, usually plays a primary role for crack initiation, this parameter was often used in the past to try to correlate the crack path of short fatigue cracks, maintaining some confusion around this question. The crack geometry imposes its own stress state, which is highly multi-axial and also depends on the relative position of the crack with respect to the crystalline orientation. On the contrary, full-field simulations using the actual geometry of both the crack and the microstructure allow to compute relevant quantities locally (like the resolved shear stress and accumulated slip on a particular slip system), which should be much more accurate to describe the crack propagation process.

3.2. Propagation of the Crack in Several Grains

To find the propagation direction, where the damage indicator reaches a maximum, at each point of the crack front, D is evaluated in a plane locally normal to the front and at a distance of 5 μm. The growth direction is taken in the direction of max(D) based on previous calculations with single crystals.[27] Using a simplified single/double configurations, it was shown that the crack was allowed to follow directions closed to the mainly activated slip system. It was also shown that the radius does not influence the results in a reasonable range (getting smaller than two elements yield unreliable results). For instance, Figure 4 show the distribution of D on both sides of the pre-crack. These distributions result on two different crack growth directions, $\theta = 81°$ in grain 6 and $\theta = 296°$ in grain 221. At each of these points, the variation of D as a function of the distance from the crack tip R_b is evaluated with respect to the threshold D_c to determine the propagation distance. It can be readily seen that the absolute value of the damage indicator will directly control the local crack growth rate. Since the distribution is evaluated locally in the vicinity of the crack front (at a given distance in a plane perpendicular to the front), the active plasticity in that region will tend to promote a faster growth rate. For instance, D is plotted after the first step on both sides of the initial crack on Figure 5a. Since the damage indicator is larger in grain 6 than in grain 221, the crack will grow more slowly on the right side than on the left side of the pre-crack.

This procedure is applied to every point along the crack front for each crack propagation step to simulate the fatigue process. A top view of the projected crack fronts after the first four crack propagation steps is shown in Figure 5b. It can be observed that the crack propagates from the initial pre-crack at different rates. At the first step of crack growth (represented by the yellow line), the crack propagation at the notch corners appears more difficult with respect to that at the free surface. Because the corners of the rectangular notch represent protruding zones, a reduced driving force is expected at these particular locations. Then, from the second crack propagation step, the crack grows all along the front with different rates. However, since everything is projected in the initial notch plane, the 3D crack shape and the grain boundary effects are difficult to infer from this figure (in grain 6 on the left side, the crack propagates upward through and crosses the boundary to enter grain 199).

The crack surface and the corresponding grains are extracted from the volume mesh after the 4th step in Figure 6. The crack surface is mapped with the inverse pole figure colors for the cubic symmetry, in order to get a visual representation of which crystallographic planes are favoured by the model. On the left side of the initial defect, the crack propagates through about 20 μm from grain 6 to grain 199. At the sample surface, the direction of crack propagation changes progressively at each crack propagation event. At the end of the second crack growth step, the crack stops in front of the grain boundary. It propagates into grain 199, almost along the same direction, which

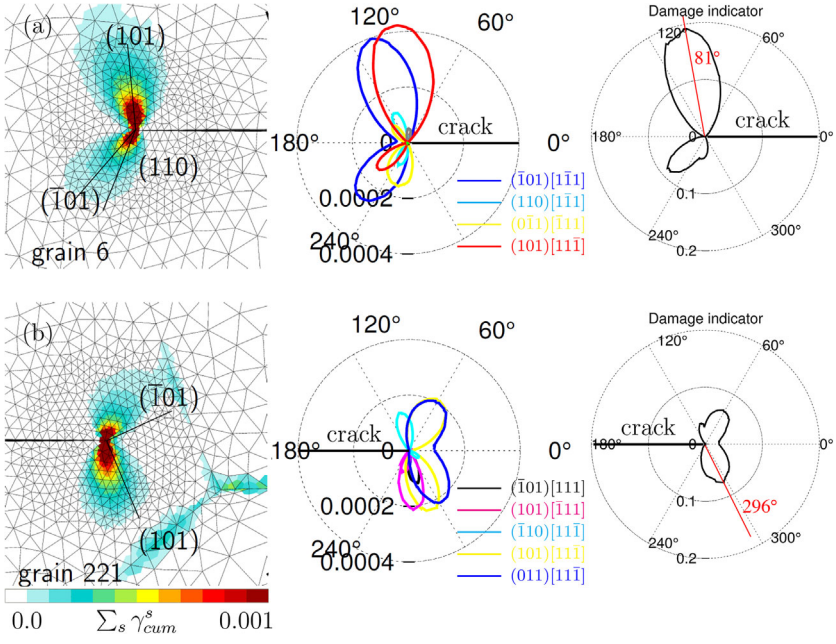

Fig. 4. Analysis of the slip activity: ac cumulated plastic strain after the first step (the intersection of some slip planes with the sample surface is displayed); radial plots show the cumulated plastic strain of the most activated slip systems and the damage indicator value (in MPa) at a radius of 5 μm around the crack tip on both sides (a) left side, grain 6 (b) right side, grain 221.

ADVANCED ENGINEERING MATERIALS 2017,
DOI: 10.1002/adem.201600721

ADVANCED ENGINEERING MATERIALS

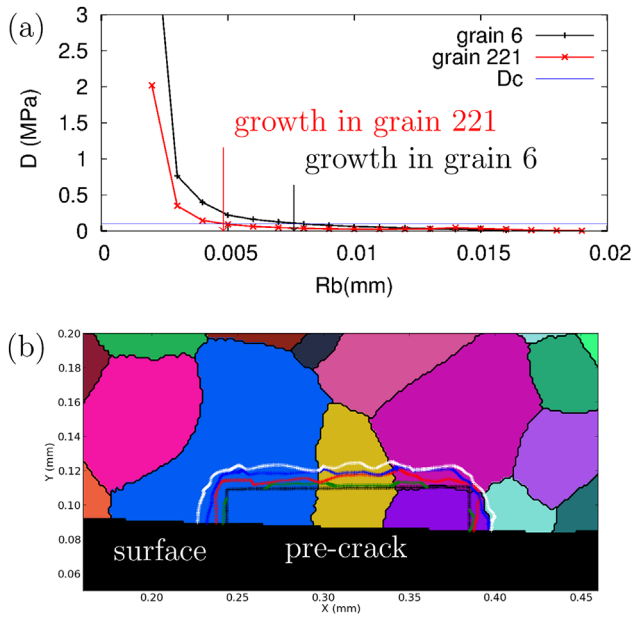

Fig. 5. (a) Damage indicator distributions along each the propagation direction in grain 6 (left side) and grain 221 (right side) showing two different propagation distances (b) result of the 4 propagation steps projected on the initial notch plane.

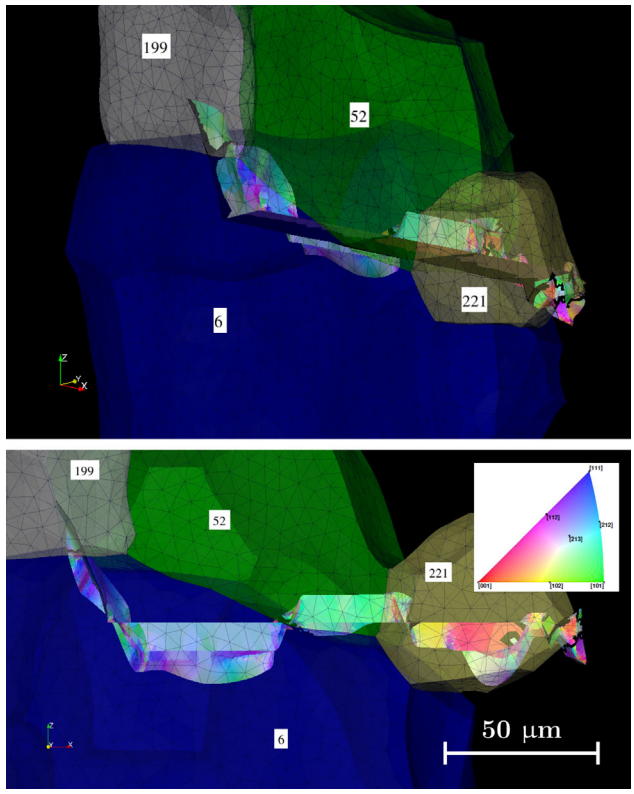

Fig. 6. (a) Crack surface and the corresponding grains at the fourth step crack propagation, (b) front view, the black lines on the crack surface represent grain boundaries.

remains close to a {110} type crystallographic plane, see Figure 6.

In the bulk of grain 6, the direction of crack propagation varies from upward to downward at the two edges of the notch corner. Moreover, the values of the damage indicator D inside grain 6 are smaller than at the surface. Indeed, the plane stress state at the surface allows more plastic deformation, which translates into larger D values. The results at different crack growth distances are shown in Figure 6a. Strong crack deflections take place at the grain boundaries between grain 6 and grain 52 and also between grain 52 and grain 221, because of the different grain orientations. As a side note, the crack is here a smooth (derivable) surface (although it can be very tortuous as shown here), which directly limit the level of details that can be simulated. A particular situation occurs, when the crack meet a grain boundary upfront and two different direction are taken in each grain (a situation, where experimentally the crack can split into two branches). Here, the crack path smoothly transition from one direction to the next (as seen in the bulk of grains 6 and 52, Figure 6b). The steepness of the transition is directly controlled by the number of points of the crack front included in the remeshing algorithm.

In some cases, crack bifurcation also occurs within the grains from one step to the next propagation step. This can be observed in grain 221, that is, at the right side of the pre-crack, in Figure 6b. The crack grows downward in the first step, and goes upward in the next step. This phenomenon is also observed inside grains 6 and 52. Several reasons can explain those bifurcations: i) the complex non symmetric grain orientation and the horizontal pre-crack induce the activation of several slip systems at the crack front. The competition between the various activated slip systems at the crack front makes the selection of crack direction more difficult. This can be observed from the small difference of the damage indicator value at the crack front shown in Figure 5b of grain 221. This situation is similar to the zig-zag crack growth obtained in a much more idealized situation of a monocrystal with two symmetric slip systems.[27] ii) Due to the high computational cost and time issues, only four propagation steps were simulated using a small value for the damage threshold D_c. This leads to a high sensitivity of the crack propagation direction, especially close to a grain boundary.

3.3. Crack Growth Rates and Influence of Grain Boundaries

The average crack growth distance at each step, which can be linked to the crack growth rate da/dN, is calculated in grains 6 and 221, where the pre-crack is mainly located. The average crack growth distances in the two grains are determined by averaging the crack growth distance, at each point of the crack front in both grains. The results of the average crack growth rate da/dN and the crack growth distance of each point as a function of the crack length are shown in Figure 7. In the results, the crack length is measured with respect to the initial defect.

Figure 7 shows that da/dN in grain 6 is higher than in grain 221. This can also be observed in Figure 6 at the sample surface. The average crack growth rates are in the order of several microns per step. The difference in the crack growth

DOI: 10.1002/adem.201600721

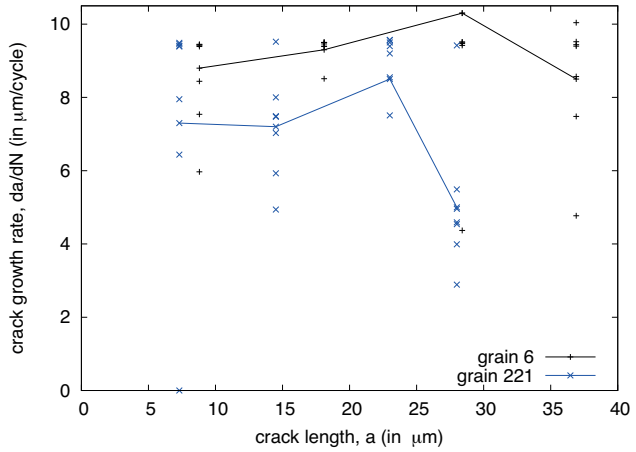

Fig. 7. Average growth rates in grain 6 and grain 221.

rates seems to be related to the pre-crack position with respect to the grain boundary and the grain orientation. From the view of the crack surface in Figure 6, it can be observed that the right side of the pre-crack front is close to the grain boundary of grain 221, that acts as a barrier against the crack propagation. On the other hand, grain 6 and subsequently grain 199 show a pronounced growth close to a {110} plane and it turns out that crossing the boundary did not imply any retardation. Indeed, the twist angle measured from the crack plane on each side of the boundary is only 4°, showing no resistance to crack propagation.

3.4. Discussion

All these results are in agreement with the general features of short cracks observed experimentally in 3D experiments, such as deviation at grain boundary and the effect of the twist angle on the crack retardation.[11,15,41,42] They could be complemented in the future to tend toward a microstructurally informed, quantitative model for short crack propagation. However, at this point, the number of propagation steps remains too limited to draw further conclusions. In the future, such simulation could be used to validate fatigue cracking models by comparing local crack growth events on a grain by grain basis as measured with in situ X-ray tomography for instance.

It is important to understand that each step capture the plastic activity at the crack tip for a given crack geometry. The central hypothesis is that, this state can be used to propagate the crack on a certain distance, typically in the order of the plastic zone size. By running several steps, it becomes possible to propagate the crack through several grains in a polycrystalline microstructure. This hypothesis will not hold for generalized plasticity or for a value of D_c to low, which would allow the crack to propagate too far from a single simulation step. From that point of view, the model should be well suited to simulate HCF and VHCF fatigue crack growth, where the microstructure has a very strong influence.[43–45] Other avenues also exist like using reduced-basis techniques to increase drastically the efficiency of the computation[46] and, thus, be able to simulate every fatigue cycle.

Several hypotheses limit the predictability of the present simulation framework: first, the use of only 12 slip systems for a BCC material, this is known to be a rather strong approximation with regard to the prediction of material descriptors,[47] but allowed to drastically reduce the number of degrees of freedom; the simulation of only one cycle for each step can as been discussed, as well as the transfer of plastic strain field from one step to the next. All of these limitations can be removed in the future with increased computational power and improvements in numerical methods. It will not change the qualitative conclusion of this work, but is necessary to compare the predictions with experimental results in order to validate a FIP criterion for short fatigue crack propagation.

4. Conclusion

This work builds upon a previously presented computational framework to simulate short crack propagation in polycrystals. In the present paper, the emphasis was put on using the polycrystalline microstructure characterized by DCT as input for the calculation.

A finite element mesh was first built from the experimental microstructure and a crystal plasticity model was used to compute a fatigue indicator parameter field. Post-processing this indicator allows to determine the propagation direction and distance for each point of the crack front.

Starting from an initial rectangular defect, the fatigue crack was propagated through several grains and showed a pronounced short crack behavior with a varying crack growth rate in different locations. The crack experiences deviation at grain boundaries and also within the grains. In one particular area, the crack closely followed a {110} plane and entered another grain switching onto another {110} plane with a very low twist angle configuration, which showed no retardation effect.

To the best of the authors knowledge, this is the first time such a calculation is achieved, and although a compromise with strong hypothesis on some of the material parameters was made to meet time constraints, this is a significant step toward the simulation of short crack propagation. In the future, comparing simulation results with detailed 3D in situ experiments could lead to a comprehensive modeling of the short crack behavior.

Article first published online: xxxx
Manuscript Revised: December 24, 2016
Manuscript Received: October 20, 2016

[1] G. M. Castelluccio, W. D. Musinski, D. L. McDowell, *Curr. Opin. Solid State Mater. Sci.* **2014**, *18*, 180.
[2] D. L. McDowell, F. P. E. Dunne, *Int. J. Fatigue* **2010**, *32*, 1521.

[3] M. D. Sangid, H. J. Maier, H. Sehitoglu, *J. Mech. Phys. Solids* **2011**, *59*, 595.
[4] J.-C. Stinville, W. C. Lenthe, J. Miao, T. M. Pollock, *Acta Mater.* **2016**, *103*, 461.
[5] K. Tanaka, Y. Akiniwa, Y. Nakai, R. P. Wei, *Eng. Fract. Mech.* **1986**, *24*, 803.
[6] K. J. Miller, *Fatigue Fract. Eng. Mater. Struct.* **1987**, *10*, 93.
[7] A. Navarro, E. R. de los Rios, *Philos. Mag.* **1988**, *57*, 15.
[8] J.-Y. Buffière, E. Ferrié, H. Proudhon, W. Ludwig, *Mater. Sci. Technol.* **2006**, *22*, 1019.
[9] P. J. Withers, M. Preuss, *Annu. Rev. Mater. Res.* **2012**, *42*, 81.
[10] F. Yoshinaka, T. Nakamura, S. Nakayama, D. Shiozawa, Y. Nakai, K. Uesugi, *Int. J. Fatigue* **2016**, *93*, 397.
[11] M. Herbig, A. King, P. Reischig, H. Proudhon, E. M. Lauridsen, J. Marrow, J.-Y. Buffière, W. Ludwig, *Acta Mater.* **2011**, *59*, 590.
[12] A. King, W. Ludwig, M. Herbig, J.-Y. Buffière, A. A. Khan, N. Stevens, T. J. Marrow, *Acta Mater.* **2011**, *59*, 6761.
[13] W. Schaef, M. Marx, H. Veho, A. Heckl, P. Randelzhofer, *Acta Mater.* **2011**, *59*, 1849.
[14] T. J. Marrow, M. Mostafavi, T. Hashimoto, G. E. Thompson, *Int. J. Fatigue* **2014**, *66*, 183.
[15] A. D. Spear, S. F. Li, J. F. Lind, R. M. Suter, A. R. Ingraffea, *Acta Mater.* **2014**, *76*, 413.
[16] M. P. Echlin, A. Mottura, C. J. Torbet, T. M. Pollock, *Rev. Sci. Instrum.* **2012**, *83*, 023701.
[17] M. P. Echlin, M. Straw, S. Randolph, J. Filevich, T. M. Pollock. *Mater. Charact.* **2015**, *100*, 1.
[18] A. Fatemi, D. F. Socie, *Fatigue Fract. Eng. Mater. Struct.* **1988**, *11*, 149.
[19] M. A. Tschopp, D. L. McDowell. *J. Mech. Phys. Solids* **2008**, *56*, 1806.
[20] J. D. Hochhalter, D. J. Littlewood, R. J. Christ Jr, M. G. Veilleux, J. E. Bozek, A. R. Ingraea, A. M. Maniatty, *Modell. Simul. Mater. Sci. Eng.* **2010**, *18*, 045004.
[21] W. D. Musinski, D. L. McDowell, *Int. J. Fatigue* **2012**, *37*, 41.
[22] C. Robert, N. Saintier, T. Palin-Luc, F. Morel, *Mech. Mater.* **2012**, *55*, 112.
[23] G. M. Castelluccio, D. L. McDowell, *Int. J. Fract.* **2012**, *176*, 49.
[24] A. King, P. Reischig, J. Adrien, S. Peetermans, W. Ludwig, *Mater. Charact.* **2014**, *97*, 1.
[25] H. Proudhon, J. Li, P. Reischig, N. Guéninchault, S. Forest, W. Ludwig, *Adv. Eng. Mater.* **2016**, *18*, 903.
[26] A. D. Spear, J. D. Hochhalter, A. R. Cerrone, S. F. Li, J. F. Lind, R. M. Suter, A. R. Ingraea, *Fatigue Fract. Eng. Mater. Struct.* **2016**, *39*, 737.
[27] H. Proudhon, J. Li, F. Wang, A. Roos, V. Chiaruttini, S. Forest, *Int. J. Fatigue* **2016**, *82*, 238.
[28] B. Künkler, O. Düber, P. Köster, U. Krupp, C.-P. Fritzen, H.-J. Christ, *Eng. Fract. Mech.* **2008**, *75*, 715.
[29] G. M. Castelluccio, D. L. McDowell, *Int. J. Fatigue* **2016**, *82*, 521.
[30] W. D. Musinski, D. L. McDowell, *Acta Mater.* **2016**, *112*, 20.
[31] W. Ludwig, A. King, P. Reischig, M. Herbig, E. M. Lauridsen, S. Schmidt, H. Proudhon, S. Forest, P. Cloetens, S. Rolland du Roscoat, J. Y. Buffière, T. J. Marrow, H. F. Poulsen, *Mater. Sci. Eng. A* **2009**, *524*, 69.
[32] W. Ludwig, P. Reischig, A. King, M. Herbig, E. M. Lauridsen, G. Johnson, T. J. Marrow, J. Y. Buffière, *Rev. Sci. Instrum.* **2009**, *80*, 033905.
[33] L. Meric, P. Poubanne, G. Cailletaud, *J. Eng. Mater. Technol.* **1991**, *113*, 162.
[34] L. Meric, G. Cailletaud, *J. Eng. Mater. Technol.* **1991**, *113*, 171.
[35] S. Fréour, E. Lacoste, M. Francois, R. Guillen, *Mater. Sci. Forum* **2011**, *681*, 97.
[36] R. Branco, F. V. Antunes, J. D. Costa, *Engineering Fracture Mechanics* **2015**, *141*, 170.
[37] J. Li, H. Proudhon, A. Roos, V. Chiaruttini, S. Forest, *Comput. Mater. Sci.* **2014**, *94*, 191.
[38] V. Chiaruttini, F. Feyel, J.-L. Chaboche. *IV European Conference on Computational Mechanics*, Paris, France **2010**. https://www.ecm-2010.org/abstract_pdf/abstract_1970.pdf
[39] V. Chiaruttini, V. Riolo, F. Feyel, *13th Int. Conf. on Fracture, Beijing, China*, Red Hook, NY, Curan Associates, Inc. **2013**.
[40] C. Farhat, F. Roux, *Int. J. Numer. Methods Eng.* **1991**, *32*, 1205.
[41] T. Zhai, A. J. Wilkinson, J. W. Martin, *Acta Mater.* **2000**, *48*, 4917.
[42] U. Krupp, *Fatigue Crack Propagation in Metals and Alloys: Microstructural Aspects and Modelling Concepts*, Weinheim, WILEY-VCH Verlag GmbH & Co, KGaA **2007**.
[43] A. C. Grigorescu, P.-M. Hilgendor, M. Zimmermann, C.-P. Fritzen, H.-J. Christ, *Int. J. Fatigue* **2016**, *93*, 250.
[44] P.-M. Hilgendor, A. C. Grigorescu, M. Zimmermann, C.-P. Fritzen, H.-J. Christ, *Int. J. Fatigue* **2016**, *93*, 261.
[45] G. M. Castelluccio, W. D. Musinski, D. L. McDowell, *Int. J. Fatigue* **2016**, *93*, 387.
[46] D. Ryckelynck, D. Missoum Benziane, *Comput Methods Appl. Mech. Eng.* **2010**, *199*, 1134.
[47] A. C. Lewis, S. M. Qidwai, A. B. Geltmacher, *Metall. Mater. Trans. A* **2010**, *41*, 2522.